

# Hybrid circuit cavity quantum electrodynamics with a micromechanical resonator

J.-M. Pirkkalainen, S. U. Cho,\* Jian Li, G. S. Paraoanu, P. J. Hakonen, and M. A. Sillanpää†  
*O. V. Lounasmaa Laboratory, Low Temperature Laboratory,  
 Aalto University, P.O. Box 15100, FI-00076 Aalto, Finland.*

Hybrid quantum systems with inherently distinct degrees of freedom play a key role in many physical phenomena. A strong coupling can make the constituents lose their individual character and form entangled states. The properties of these collective excitations, such as polaritons of light and phonons in semiconductors, can combine the benefits of each subsystem. In the emerging field of quantum information control, a promising direction is provided by the combination between long-lived atomic states<sup>1,2</sup> and the accessible electrical degrees of freedom in superconducting cavities and qubits<sup>3,4</sup>. Here we demonstrate the possibility to integrate circuit cavity quantum electrodynamics<sup>5,6</sup> with phonons. Besides coupling to a microwave cavity, our superconducting transmon qubit interacts with a resonant phonon mode in a micromechanical resonator, allowing the combination of long lifetime, strong tunable coupling, and ease of access. We measure the phonon Stark shift, as well as the splitting of the transmon qubit<sup>7</sup> spectral line into motional sidebands representing transitions between electromechanical polaritons formed by phonons and the qubit. In the time domain, we observe coherent sideband Rabi oscillations between the qubit states and phonons. This advance may allow for storage of quantum information in long-lived phonon states, and for investigations of strongly coupled quantum systems near the classical limit.

Superconducting quantum bits based on Josephson junctions<sup>4</sup> have offered an unparalleled testing ground for quantum mechanics in relatively large systems. At the same time, Josephson devices represent a promising implementation for quantum information processing. Basic quantum algorithms have indeed been recently demonstrated with both phase<sup>8</sup> as well as transmon<sup>9–11</sup> qubits. The latter operate in the circuit cavity quantum electrodynamics (QED) architecture, in which the qubits couple to an on-chip<sup>5</sup> or 3-dimensional microwave cavity resonator<sup>12</sup>. The circuit QED setup, which enables coupling of qubits and non-destructive measurements of quantum states, can be regarded as the most feasible platform.

The forthcoming challenges include the storage and retrieval of qubit states in a long-lived quantum memory. Hybrid quantum systems, where macroscopic qubits are coupled to spin ensembles, are showing promise due to their long lifetime<sup>13,14</sup>, but with the drawback of a difficult access and small coupling at the level of a single atomic degree of freedom. Another important challenge is the quantum communication<sup>15,16</sup> between spatially separated superconducting qubits.

Micromechanical resonators were brought to the quantum regime of their motion only very recently<sup>17,18</sup>, and their coupling to Josephson junction qubits<sup>19–21</sup> has high potential to achieve the aforementioned goals. The first experiment of this kind demonstrated the interaction between a charge qubit and a beam resonating at the frequency  $\omega_m/2\pi \sim 60$  MHz<sup>22</sup>. This experiment, using a read-out via the micromechanical device, did not allow for time-resolved measurements, a pre-requisite for coherent state transfer. The resonant coupling was recently demonstrated with a microwave-regime piezoelec-

tric device<sup>23</sup>, having  $\omega_m/2\pi \sim 6.2$  GHz, but the energy decay times were unfortunately very short due to high mechanical frequency and special materials.

Our approach to improve on these issues is to utilize a membrane-type micromechanical resonator embedded in a complete circuit QED device. Our aim is also to further the understanding of the physics of slowly moving bodies close to the quantum limit, as well as the emergence of ultrastrong coupling of a micromechanical phonon degree of freedom, representing matter, to microwave light.

On the conceptual level, our device is analogous to an optical cavity QED system where a two-level atom is coupled to two cavities having different frequencies (see Fig. 1a). We use a superconducting transmon qubit<sup>7</sup>, with the capacitance  $C_q$ , single-electron charging energy  $E_C \simeq e^2/2C_q$  and Josephson energy  $E_J$  as an artificial two-level system. It is coupled to a highly detuned phononic cavity formed by a suspended aluminum membrane (Fig. 1d) with  $\omega_m/(2\pi) \sim 72$  MHz by means of a position-dependent capacitance  $C_g(x)$ , as well as to a nearly resonant photonic cavity realized as an on-chip coplanar waveguide microwave resonator with frequency  $\omega_c$ .

The equivalent electrical circuit (Fig. 1b) for the two-resonator circuit QED system allows writing the Hamiltonian

$$\hat{H} = \hat{H}_q + \hbar\omega_c(\hat{a}^\dagger\hat{a} + 1/2) + \hbar\omega_m(\hat{b}^\dagger\hat{b} + 1/2) + \hbar g_c(n_0 - \hat{n})(\hat{a}^\dagger + \hat{a}) + \hbar g_m(n_0 - \hat{n})(\hat{b}^\dagger + \hat{b}), \quad (1)$$

where  $\hat{H}_q$  is the qubit Hamiltonian (see Supplementary),  $\hat{a}$  and  $\hat{b}$  are the annihilation operators of the microwave cavity and of the mechanical resonator, respectively, and  $\hat{n}$  is the number operator of Cooper pairs on the transmon

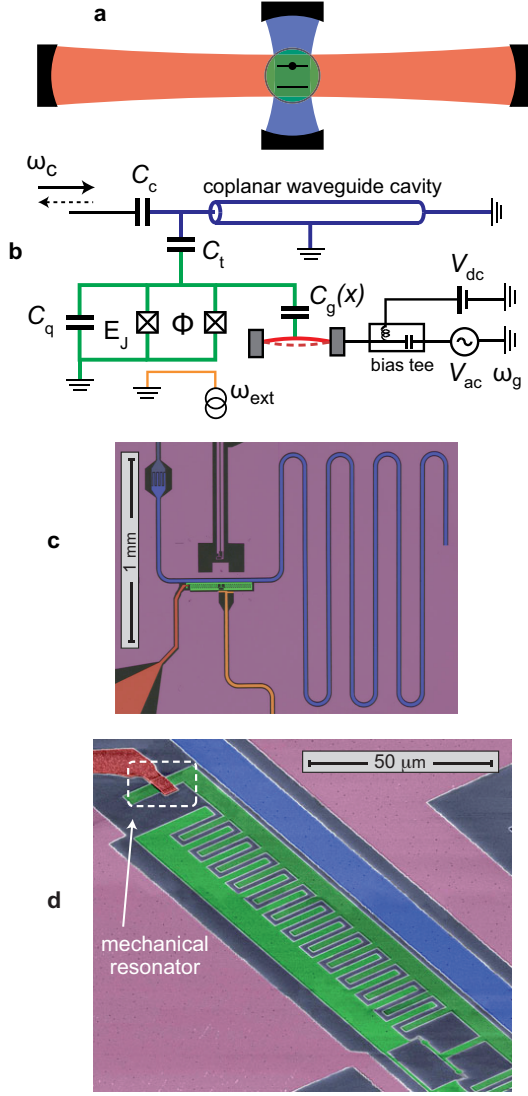


FIG. 1: **Hybrid QED setup.** **a**, Illustration of a cavity quantum electrodynamics (QED) system consisting of an atom (green) coupled to two cavities. Blue color corresponds to the (photonic) microwave resonator and red to the (phononic) lower-frequency mechanical resonator. **b**, Circuit schematics of an analogous electromechanical tripartite system, measured via a microwave cavity with a probe tone at frequency  $\omega_c$ . **c**, Optical image of the chip. Shown is the quarter-wavelength microwave cavity, the superconducting transmon qubit playing the role of the atom, the mechanical resonator with its external control, a flux control line (orange), and the ground plane (magenta). **d**, Scanning electron micrograph showing the 5  $\mu m$  long and 4  $\mu m$  wide bridge-type mechanical resonator (dashed box) suspended above the qubit island.

island. The qubit-mechanics interaction is given by the electromechanical coupling energy  $\hbar g_m = x_{zp} V_{dc} \frac{dC_g}{dx} \frac{2e}{C_q}$ . Here,  $x_{zp}$  is defined as the mechanical zero-point motion,  $V_{dc}$  is a constant voltage applied to the mechanical resonator, and  $n_0 = C_g V_{dc} / 2e$  is the dimensionless gate

charge. The coupling between the qubit and the cavity, characterized by the energy  $\hbar g_c$ , allows for a dispersive measurement of the state of the qubit using the state-dependent pull on the cavity<sup>24</sup>.

We use the three lowest energy eigenstates of the transmon qubit, labeled as the ground state  $|g\rangle$ , and the first and second excited states  $|e\rangle$  and  $|f\rangle$ , respectively. The corresponding transition frequencies, tunable in the GHz regime by flux bias  $\Phi_{dc}$ , are  $\omega_{g-e}$  and  $\omega_{e-f}$ . Somewhat different from the standard concept of a qubit, which usually involves the ground state, we treat  $|e\rangle$  and  $|f\rangle$  as the two-level system. This is beneficial, because the phonon coupling grows for higher levels of the qubit.

The coupling of the qubit to the phonons in the mechanical resonator in Eq. (1) is described by a generic light-matter interaction. The quantum states of this coupled system are dressed states, which are combinations of the qubit and of the mechanical resonator Fock states  $|N_m\rangle$  with phonon number  $N_m$ . For high  $N_m$  the effective coupling  $g_m \sqrt{N_m + 1}$  becomes comparable to the qubit frequency, and the states attain a highly entangled character as electromechanical polaritons. Similarly, the qubit transition frequencies are expected to depend on the number of quanta (ac Stark shift). As a phonon-induced effect, it was measured indirectly through the mechanics<sup>22</sup>. One can calculate the phonon Stark shift of the frequency  $\omega_{e-f}$  of the  $|e\rangle$ - $|f\rangle$  transition going beyond the linear regime:

$$\Delta\omega_{e-f}/2\pi = -\frac{\epsilon_{e-f}}{2} \cos(2\pi n_0) [J_0(2\pi n_x) - 1], \quad (2)$$

where the argument of the Bessel function is the motional gate charge amplitude  $n_x = \left(\frac{\hbar g_m}{4E_C}\right) \sqrt{N_m}$ , and the charge dispersion of the transmon qubit is  $\epsilon_{e-f} \simeq E_C \frac{2^{4m+5}}{m!} \sqrt{\frac{2}{\pi}} \left(\frac{E_J}{2E_C}\right)^{\frac{m}{2} + \frac{3}{4}} \exp\left(-\sqrt{8E_J/E_C}\right)$ , with  $m = 3$  for this transition. The shift grows first linearly with the phonon number, according to  $\Delta\omega_{e-f} \simeq \frac{\epsilon_{e-f}}{2} \pi^2 \cos(2\pi n_0) \left(\frac{\hbar g_m}{4E_C}\right)^2 N_m$ .

The device (see Fig. 1c,d) was fabricated out of aluminum on a sapphire substrate in a process comprising three layers of electron-beam lithography. In order to suspend the mechanical resonator, we used organic resist as a sacrificial layer<sup>25</sup> (see Supplementary). The quarter-wavelength microwave cavity has a resonant frequency of  $\omega_c/2\pi = 4.84$  GHz, coupling to the qubit capacitively at the rate  $g_c/2\pi = 100$  MHz. The cavity is coupled to the measurement circuitry by a large input/output capacitor resulting in the external linewidth  $\gamma_E/2\pi \simeq 15$  MHz. The device is mounted in a dilution refrigerator at a temperature of  $T = 25$  mK. Although we did not access the thermal phonon number, we expect the membrane to thermalize<sup>17</sup> down to the thermal occupancy  $N_m^T = k_B T / \hbar \omega_m \lesssim 10$ .

We first identified the lowest mechanical eigenmode of the membrane. The electromechanical interaction was

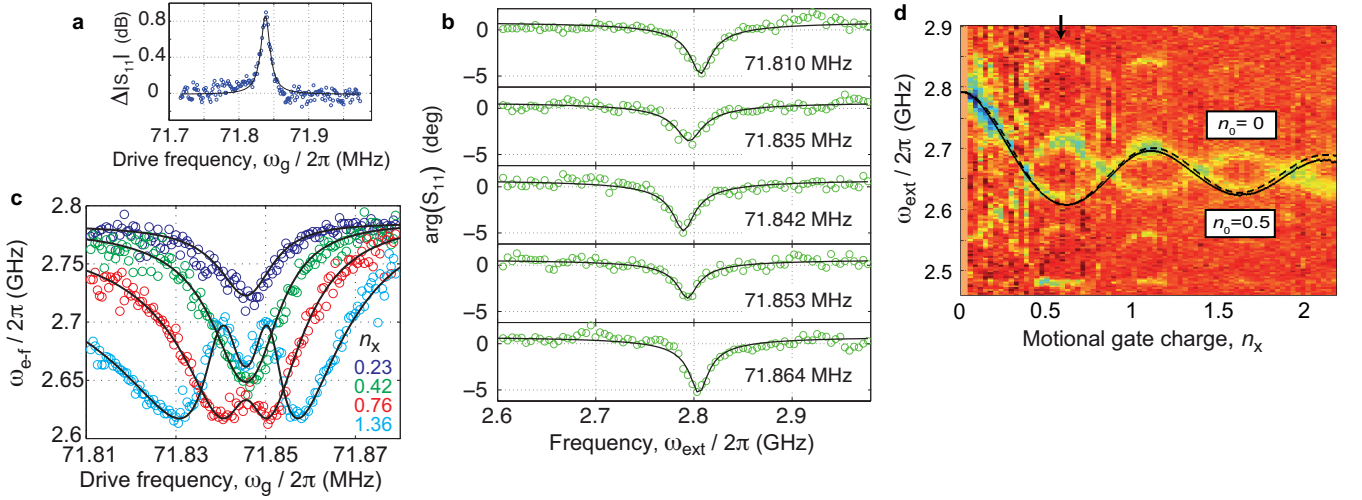


FIG. 2: **Phonon Stark shift.** **a**, The driven mechanical resonance appears as enhanced absorption in a single-tone cavity spectroscopy. **b**, In two-tone spectroscopy (flux bias  $\Phi_{dc}/\Phi_0 = 0.368$ , and  $n_0 = 0.5$ ) the dip representing the transition  $|e\rangle$ - $|f\rangle$  (between the first and second excited states) of the transmon qubit, is observed to red-shift when the mechanical drive frequency is swept across resonance. Circles denote the phase of the cavity reflection, and the solid lines are Lorentzian fits. With resonant mechanical drive  $\omega_g/2\pi = \omega_m/2\pi = 71.842$  MHz, a mechanical motion is excited with an amplitude of 220 fm, about 80 times  $x_{zp}$ , and the phonon number  $N_m \sim 6 \times 10^3$ . In gate charge units, this equals a motional gate charge  $n_x = 0.09$ . **c**, Shift of the qubit transition at flux bias  $\Phi_{dc}/\Phi_0 = 0.370$  as a function of driving frequency, with four drive amplitudes as labeled. Circles denote the center of the dip extracted from the data as in **b**, and the solid lines are the modeled response of a mechanical resonator with  $Q_m = 5500$ . **d**, Highly non-linear regime of the phonon Stark shift with resonant drive at  $n_0 = 0$ . Due to a single electron fluctuating on and off the island, also the transition line corresponding to  $n_0 = 0.5$  is visible as a mirror image. The black dashed line is a result of full numerical Floquet modeling, and the dashed white line is Eq. (2).

switched on by applying a dc voltage  $V_{dc} = 5$  V, which permits an electromechanical coupling  $g_m/2\pi = 2.5$  MHz. The mechanics was driven strongly by an additional ac tone combined into a bias-T inside the cryostat as shown in Fig. 1b. When the qubit is biased near the microwave cavity resonance, the cavity absorption in a single-tone measurement is altered when the mechanical mode is excited. This way, we obtain the mechanical peak at  $\omega_m/2\pi = 71.842$  MHz, as displayed in Figure 2a.

By virtue of different frequency ranges of the qubit and the mechanical resonator, we cannot bring them on resonance by tuning the qubit frequency with a flux bias. A highly detuned regime, analogously to trapped ions<sup>1,26,27</sup>, nonetheless allows for complete quantum control. The pertinent phenomena are the Stark shift of the qubit transition frequency, and sideband transitions.

A two-tone spectroscopy is used to investigate the qubit  $|e\rangle$ - $|f\rangle$  transition for detecting the Stark shift. A standard method to probe this transition is to start by applying resonant microwaves in order to excite the qubit from the ground state  $|g\rangle$  to  $|e\rangle$ . However, it turns out that in our system a small but nonzero population exists on  $|e\rangle$  even in equilibrium, thus an initial excitation is not necessary. The actual excitation microwave tone (frequency  $\omega_{ext}$ ) is applied to the transmon flux coil, and the increased population of the level  $|f\rangle$  is distinguished as a phase shift of the probe tone. A shift of  $\Delta\omega_{e-f}/2\pi = -18$

MHz in Fig. 2b from the bare value  $\omega_{e-f}/2\pi = 2.81$  GHz can be attributed to the phonon-induced Stark shift.

We can extract the center of the  $|e\rangle$ - $|f\rangle$  transition dip and vary the motion amplitude, as shown in Fig. 2c. A slight difference of the bare value to that in Fig. 2b is due to a flux offset of  $\sim 2$  m $\Phi_0$ . Towards increasing vibration amplitude, the shift becomes more pronounced, and thereafter assumes a highly nonlinear and oscillatory behavior when the motional gate charge reaches values of the order  $n_x \gtrsim 0.5$ . This rather extreme regime can be explored by fixing a resonant mechanical drive, as implemented in the measurement shown in Fig. 2d. This data shows the Bessel-type oscillatory Stark shift, in accord with Eq. (2).

To model the shift, we first note that the total time-dependent gate charge is comprised of two components:  $\Delta n_g = n_x + C_g V_{ac}/2e$ , where the second term is a cross talk from the ac voltage drive on the mechanics. On resonance, the latter contributes 8 % of  $n_x$ . Since the two terms have opposite phases when the drive is below/above  $\omega_m$ , they sum up to make the Stark shift asymmetric, as clearly seen in Fig. 2c. We used the motional gate charge  $n_x$  at the frequency  $\omega_m$  as a common fitting parameter. The analytic result in Eq. (2) already gives an excellent agreement with the measurement, as shown in Fig. 2d. Beyond analytics, we made a complete numerical calculation using a Floquet modeling of the

full transmon Hamiltonian (see Supplementary), matching well the observed spectroscopy in Fig. 2c,d.

The excellent match to the theory clearly vindicates the phonon origin of the Stark shift. On top of that, the highly non-linear shift can be seen as a manifestation of ultrastrong coupling from light to matter<sup>28,29</sup>. Indeed, the frequency shift due to coupling goes far beyond the linear regime, exceeding the bare mechanical frequency.

We can use sideband transitions to transfer quanta between the qubit and the mechanical resonator<sup>26,27</sup>. More specifically, the transitions occur between the entangled dressed states. However, an intuitive appealing picture is to describe them by using uncoupled states  $|e, N_m\rangle$ ,  $|f, N'_m\rangle$ , see Fig. 3a. With the parameter choice in Fig. 3b, the transmon charge dispersion and effective coupling are large enough so that the basis states are entangled electromechanical polariton states. In Fig. 3c, the effective coupling is smaller such that the description in terms of separable qubit and phonon states is valid.

Since the data of Fig. 3b were taken at the gate charge extreme offsets ( $n_0 = 0, 0.5$ ), we obtain only two-phonon processes due to symmetry reasons. However, offset drift during data taking rendered the first order sidebands visible in Fig. 3b. As the Rabi frequency is relatively low in Fig. 3b, we can use an analytical result for the qubit population, obtaining an excellent agreement with the measured sidebands. Under proper phonon occupancy, we also can eliminate dephasing due to gate charge fluctuations, as well as the fluctuating quasiparticle.

For investigating the energy exchange in the time domain, we performed time-resolved measurements in the setup of Fig. 3c. Here, instead of a continuous microwave irradiation as in the two-tone spectroscopy of Figs. 2 and 3, we pulsate the excitation microwave tone at varying widths, while monitoring the level  $|f\rangle$  population. During the pulse, the system is expected to coherently evolve at the Rabi frequency  $\Delta_k$  (for sideband  $k$ ) between a pair of eigenstates as illustrated by arrows in Fig. 3a. Figures 4a,b show the obtained Rabi oscillations on the bare qubit transition ( $k = 0$ ) and on the first blue sideband ( $k = 1$ ). The latter indicate that the qubit can swap the state while simultaneously adding or removing one quantum in the mechanical resonator, thereafter, converting the information into flying microwave photons in the non-destructive measurement process. We can map this energy exchange by varying the detuning of the excitation microwave (Fig. 4c), as well as by converting the data to frequency domain (Fig. 4d). The data shows, as expected, an increase of the Rabi frequency on detuning from a particular sideband. However, the same theory, which supposes non-overlapping of the peaks, cannot be used to relate the peak widths in Fig. 3c to the Rabi frequencies.

The phonon-photon conversion demonstrated here forms a building block for the conversion of quantum information between microwave light and mechanical mo-

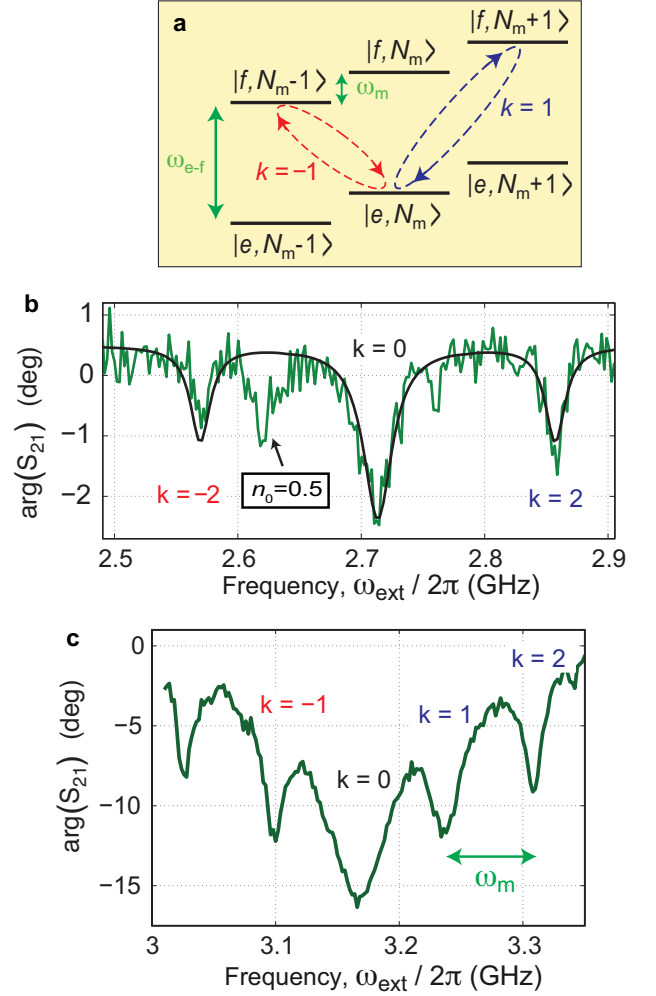


**FIG. 3: Motional sideband transitions.** **a**, In a Stokes (red sideband) scattering event, the qubit exchanges (absorbs/emits) a quantum of frequency  $\omega_{e-f} + k\omega_m$  with the microwave field, whereas the mechanics emits/absorbs  $k$  quanta. In an anti-Stokes (blue sideband) scattering event, the process is reversed. **b**, Cross-cut along the dashed vertical line from Fig. 2d at  $n_x \simeq 0.6$ . The solid black line is a fit from the analytical model presented in the Supplementary, with decay rate  $\gamma/2\pi = 3$  MHz, dephasing rate  $\gamma_\varphi/2\pi = 6$  MHz, and main peak Rabi frequency  $\Delta_0/2\pi = 7$  MHz. **c**, Spectroscopy with the motional gate charge corresponding to the dynamical sweet spot ( $n_x = 0.4$ , see Supplementary), where the qubit is insensitive to offset charge fluctuations,  $\Phi_{\text{dc}}/\Phi_0 = 0.326$ . The qubit was driven hard at  $\Delta_0/2\pi = 31$  MHz, making the main peak broad.

tion. It also opens up the possibility of quantum memory operation. While here the storage time is limited by the thermal coherence time of the mechanics  $\tau_T = Q_m \omega_m / N_m^T \sim 1 \mu\text{s}$ , we note the encouraging recent findings<sup>30</sup> with  $Q_m \sim 10^{10}$  and  $\tau_T$  of the order seconds. This kind of micromechanical device could further allow for quantum communication by converting phonons into flying photons using radiation pressure coupling, natu-



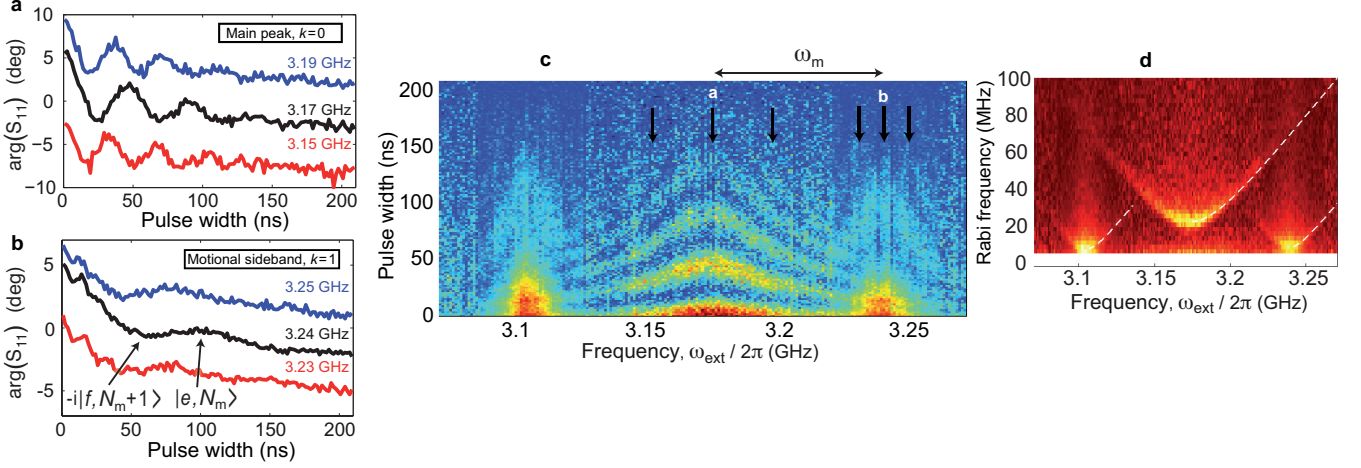


FIG. 4: **Electromechanical Rabi oscillations.** **a**, Oscillations of the phase shift of the probe tone, proportional to the population of the qubit third level  $|f\rangle$ , measured near the bare qubit frequency  $k = 0$ . Traces are offset for clarity. **b**, Time-resolved evolution between phonons and qubit states, near the first blue sideband  $k = 1$ , with the resonant Rabi frequency  $\Delta_1/2\pi \simeq 9.4$  MHz. The quantum states on the course of the evolution are marked. **c**, Qubit population oscillations mapped as a function of the qubit excitation frequency and Rabi pulse width. The traces in **a** and **b** are along the arrows. The decay time constant, related to total decoherence rate, is  $\sim 70$  ns. **d**, Fourier transform of **c** showing the Rabi frequencies of each sideband growing as a function of excitation detuning. The lines are fits to the expression  $\Delta_k(\omega_{\text{ext}}) = \sqrt{\Delta_k^2 + (\omega_{e-f} - \omega_{\text{ext}} - k\omega_m)^2}$ .

rally suited for a membrane mirror. An increase of the electromechanical coupling by means of a narrower vacuum gap and a smaller qubit capacitance could progress the interaction between light and true matter all the way into the single-phonon ultrastrong regime. The motional sideband operations also facilitate the use of the full quantum toolbox developed in the field of trapped ions<sup>1,26,27</sup> for engineering non-classical states of mechanical resonators, or long-distance entanglement of several slowly moving purely mechanical objects.

\* Present address: Korea Research Institute of Standards and Science, Daejeon 305-340, Republic of Korea

† Present address: Department of Applied Physics, Aalto University School of Science, P.O. Box 11100, FI-00076 Aalto, Finland

- [1] Leibfried, D., Blatt, R., Monroe, C. & Wineland, D. Quantum dynamics of single trapped ions. *Rev. Mod. Phys.* **75**, 281–324 (2003).
- [2] Andre, A. *et al.* A coherent all-electrical interface between polar molecules and mesoscopic superconducting resonators. *Nature Physics* **2**, 636–642 (2006).
- [3] Nakamura, Y., Pashkin, Y. A. & Tsai, J. S. Coherent control of macroscopic quantum states in a single-Cooper-pair box. *Nature* **398**, 786–788 (1999).
- [4] Clarke, J. & Wilhelm, F. K. Superconducting quantum bits. *Nature* **453**, 1031–1042 (2008).
- [5] Wallraff, A. *et al.* Strong coupling of a single photon to a superconducting qubit using circuit quantum electrodynamics. *Nature* **431**, 162–167 (2004).
- [6] Chiorescu, I. *et al.* Coherent dynamics of a flux qubit coupled to a harmonic oscillator. *Nature* **431**, 159–162

(2004).

- [7] Koch, J. *et al.* Charge-insensitive qubit design derived from the Cooper pair box. *Phys. Rev. A* **76**, 042319 (2007).
- [8] Mariani, M. *et al.* Implementing the Quantum von Neumann Architecture with Superconducting Circuits. *Science* **334**, 61–65 (2011).
- [9] Reed, M. D. *et al.* Realization of three-qubit quantum error correction with superconducting circuits. *Nature* **482**, 382–385 (2012).
- [10] Fedorov, A., Steffen, L., Baur, M., da Silva, M. P. & Wallraff, A. Implementation of a Toffoli gate with superconducting circuits. *Nature* **481**, 170–172 (2012).
- [11] Dewes, A. *et al.* Quantum speeding-up of computation demonstrated in a superconducting two-qubit processor. *Phys. Rev. B* **85**, 140503 (2012).
- [12] Paik, H. *et al.* Observation of High Coherence in Josephson Junction Qubits Measured in a Three-Dimensional Circuit QED Architecture. *Phys. Rev. Lett.* **107**, 240501 (2011).
- [13] Zhu, X. *et al.* Coherent coupling of a superconducting flux qubit to an electron spin ensemble in diamond. *Nature* **478**, 221–224 (2011).
- [14] Kubo, Y. *et al.* Hybrid quantum circuit with a superconducting qubit coupled to a spin ensemble. *Phys. Rev. Lett.* **107**, 220501 (2011).
- [15] Ursin, R. *et al.* Entanglement-based quantum communication over 144 km. *Nat. Phys.* **3**, 481–486 (2007).
- [16] Moehring, D. L. *et al.* Entanglement of single-atom quantum bits at a distance. *Nature* **449**, 68–71 (2007).
- [17] Teufel, J. D. *et al.* Sideband cooling of micromechanical motion to the quantum ground state. *Nature* **475**, 359–363 (2011).
- [18] Chan, J. *et al.* Laser cooling of a nanomechanical oscillator into its quantum ground state. *Nature* **478**, 89–92 (2011).

- [19] Armour, A. D., Blencowe, M. P. & Schwab, K. C. Entanglement and Decoherence of a Micromechanical Resonator via Coupling to a Cooper-Pair Box. *Phys. Rev. Lett.* **88**, 148301 (2002).
- [20] Tian, L. Entanglement from a nanomechanical resonator weakly coupled to a single Cooper-pair box. *Phys. Rev. B* **72**, 195411 (2005).
- [21] Etaki, S. *et al.* Motion detection of a micromechanical resonator embedded in a d.c. SQUID. *Nat. Phys.* **4**, 785–788 (2008).
- [22] LaHaye, M. D., Suh, J., Echternach, P. M., Schwab, K. C. & Roukes, M. L. Nanomechanical measurements of a superconducting qubit. *Nature* **459**, 960–964 (2009).
- [23] O’Connell, A. D. *et al.* Quantum ground state and single-phonon control of a mechanical resonator. *Nature* **464**, 697–703 (2010).
- [24] Blais, A., Huang, R.-S., Wallraff, A., Girvin, S. M. & Schoelkopf, R. J. Cavity quantum electrodynamics for superconducting electrical circuits: An architecture for quantum computation. *Phys. Rev. A* **69**, 062320 (2004).
- [25] Li, T. F. *et al.* High-frequency metallic nanomechanical resonators. *Applied Physics Letters* **92**, 043112 (2008).
- [26] Monroe, C., Meekhof, D. M., King, B. E. & Wineland, D. J. A Schrödinger Cat Superposition State of an Atom. *Science* **272**, 1131–1136 (1996).
- [27] Roos, C. *et al.* Quantum State Engineering on an Optical Transition and Decoherence in a Paul Trap. *Phys. Rev. Lett.* **83**, 4713–4716 (1999).
- [28] Niemczyk, T. *et al.* Circuit quantum electrodynamics in the ultrastrong-coupling regime. *Nat. Phys.* **6**, 772–776 (2010).
- [29] Tuorila, J. *et al.* Stark Effect and Generalized Bloch-Siegert Shift in a Strongly Driven Two-Level System. *Phys. Rev. Lett.* **105**, 257003 (2010).
- [30] Goryachev, M. *et al.* Extremely Low-Loss Acoustic Phonons in a Quartz Bulk Acoustic Wave Resonator. *arXiv:1202.4556v1* (2012).

**Acknowledgements** We thank Matti Silveri and Tero Heikkilä for useful discussions. This work was supported by the Academy of Finland and by the European Research Council (grant number 240387-NEMSQED) and EU-FP7-NMP-246026. J.-M.P. acknowledges support from Väisälä Foundation, Emil Aaltonen Foundation, and Kaute Foundation.

**Author contributions** M.A.S. conceived the experiment and designed the experimental set-up with P.J.H. J.L., J.-M.P., and G.S.P. designed the circuit layout. S.U.C. and J.-M.P. fabricated the samples. J.-M.P. conducted the measurements, developed theory and wrote the manuscript. S.U.C. supported the measurements. All authors commented on the manuscript.

**Additional information** The authors declare no competing financial interests. Supplementary information accompanies this paper on [www.nature.com/](http://www.nature.com/). Reprints and permissions information is available online at <http://www.nature.com/reprints>. Correspondence and requests for materials should be addressed to J.-M.P.

# Hybrid circuit cavity quantum electrodynamics with a micromechanical resonator: Supplementary information

J.-M. Pirkkalainen, S. U. Cho, Jian Li, G. S. Paraoanu, P. J. Hakonen, M. A. Sillanpää

O. V. Lounasmaa Laboratory, Low Temperature Laboratory, Aalto University, P.O. Box 15100, FI-00076 Aalto, Finland.

## DEVICE FABRICATION

The fabrication (Fig. S1) includes three layers of electron-beam lithography on a sapphire substrate. The first lithography patterns everything else except the mechanical resonator. Aluminum is deposited by shadow evaporation at thicknesses of 20 nm and 40 nm, with an oxidation in between in order to create the Josephson tunnel junctions.

The sacrificial layer separating the bridge from the transmon island is defined with PMMA used as a negative resist. We start by spin-coating 3 % 950k PMMA, creating about 200 nm thick layer. Under high electron dose, here 9 mC/cm<sup>2</sup> at 200 pA, PMMA cross-links, shrinks in thickness down to about 40 % and becomes insoluble. After the exposure, the non-exposed PMMA is washed away with acetone.

For the third lithography, a 800 nm thick resist serves as the deposition mask for 300 nm Al defining the mechanical resonator. After lift-off, 90 min of isotropic O<sub>2</sub> ashing at 1 Torr removes the PMMA and suspends the bridge. Although the ashing takes time, no appreciable change to qubit properties can be attributed to it.

A highly tilted SEM micrograph (Fig. S1b) reveals an undulating vacuum gap of about 40...100 nm between the bridge and the qubit island. Apparently, the PMMA thickness became non-uniform during the cross-linking. This makes it difficult to calculate  $\partial_x C_g$  from the geometry, however, the fitted value  $\partial_x C_g = 26$  nF/m is in the proper range.

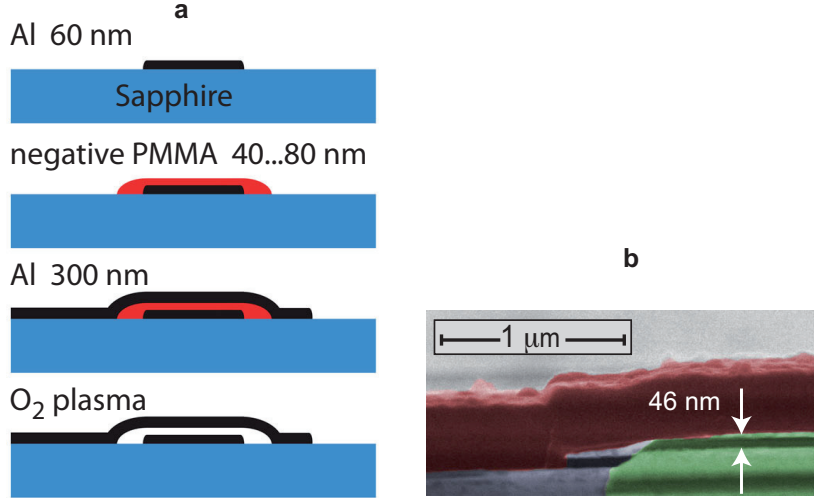


FIG. S1: **Device fabrication.** **a**, Steps (from top to bottom) of the process. **b**, Grating angle scanning electron micrograph of the mechanical resonator (red) above the superconducting qubit island (green).

## BASIC CHARACTERIZATION

With the electromechanical coupling set to zero by  $V_{dc} = 0$ , we first characterized the basic operation of the transmon-cavity circuit QED system. In Fig. S2a we show a single-tone spectroscopy, with the avoided crossings at roughly  $\Phi_{dc}/\Phi_0 \simeq \pm 0.1$ , where the qubit frequency crosses the cavity. In fact, the crossing just barely takes place, since the maximum qubit frequency is 5.0 GHz at  $\Phi_{dc} = 0$ . The wings, absent in the ideal case, around the crossing points are attributed to higher transitions in the coupled system. We expect them to be due to microwave leakage via the high gate capacitance.

Two-tone spectroscopy is the main tool used in the measurements described in the main text. It is the best way to reveal the un-dressed qubit spectral lines when far-detuned from the cavity. Fig. S2b displays such characterization over a large span of flux biases and qubit frequencies. By overlaying the results from numerical modeling, the spectral lines can be distinguished as  $|g\rangle\text{--}|e\rangle$  and  $|e\rangle\text{--}|f\rangle$  transitions. We adjusted the gate voltage such that  $n_0 = 0$ , however, especially the  $|e\rangle\text{--}|f\rangle$  line can be identified having split into two. The other branch ( $n_0 = 1/2$ ) corresponds to an extra quasiparticle on the island, excited likely by microwave leakage.

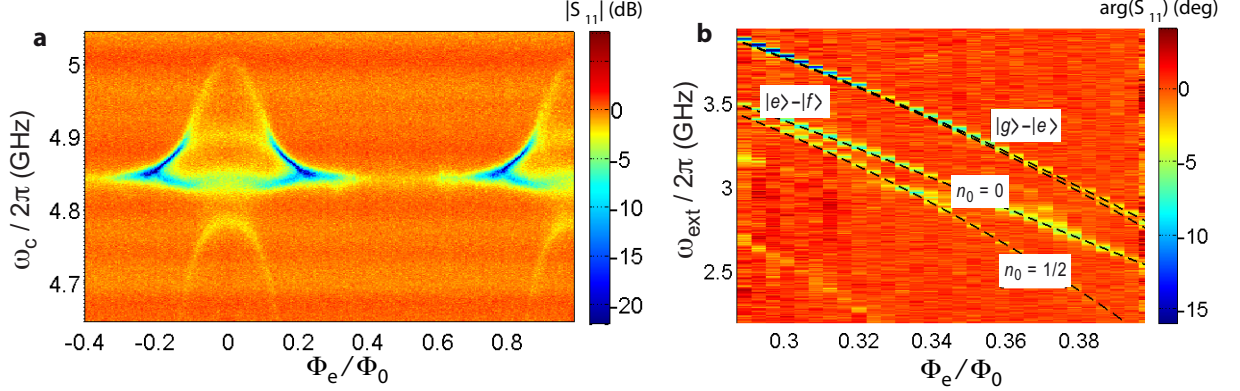


FIG. S2: **Qubit spectroscopy.** **a**, One-tone spectroscopy of the cavity resonance absorption, while the effective Josephson energy is tuned by flux bias. **b**, Two-tone spectroscopy, where the probe tone  $\omega_c$  is kept fixed near the bare cavity frequency (4.84 GHz), and qubit excitation frequency is swept. The dashed lines are the calculated transitions as labeled.

The data of Fig. S2 also allows for accurate fitting of the qubit parameters; we obtain  $E_{J1} = 4.63$  GHz,  $E_{J2} = 6.43$  GHz,  $C_q = 61$  fF,  $E_C = 318$  MHz, and the coupling energy to the microwave cavity  $g_c \simeq 100$  MHz.

The dc voltages applied to the mechanical resonator (acting also as a gate electrode to the qubit) make the background charge of the qubit more prone to jumps than without the dc voltage. We applied a slow digital feedback about once a minute to the gate in order to correct for the jumps. For this, we repeated a sequence consisting of measurement of the gate periodicity, followed by a small voltage offset, until the original offset was reached.

The mechanical Q-value of the present sample  $Q_m \simeq 5500$  is clearly lower than typically recorded ( $\gtrsim 10^5$ ) with aluminum beams<sup>1</sup> or membranes<sup>2</sup> at cryogenic temperatures. We believe this is due to either clamping losses, or the oxygen ashing changing material properties. However, the NIST design<sup>2</sup> for aluminum membrane, with  $Q_m \simeq 3 \times 10^5$  could equally well integrate in the present setup, allowing for longer storage times of qubit states in the mechanics.

## DATA ANALYSIS

The gate capacitance to the qubit,  $C_g = 1.76$  fF, is extracted from the gate charge  $n_0 = C_g V_{\text{dc}} / (2e)$  periodicity of the qubit transitions. Using the modeling of Stark shift asymmetry in Fig. 2c in main text, we can deduce the gate charge amplitude due to the direct driving. The driving voltage amplitude can then be calculated with the capacitance to the qubit. Therefore, the fitted gate charge amplitude due to the mechanical capacitance modulation translates into the derivative of the capacitance with respect to the distance,  $\partial_x C_g = 26$  nF/m. This in turn gives the coupling between the qubit and the mechanical resonator to be  $g_m / 2\pi = 5.0$  MHz with  $V_{\text{dc}} = 10$  V which was the maximum voltage applied to the device. The obtained values of the driving voltage agree well with the estimated attenuation of the drive cable, although the latter has inaccuracies of several dB.

Next, we discuss additional data on the phonon Stark shift. In figure S3, the gate charge is tuned to  $n_0 = 0.25$ , at which point the qubit transition frequency is insensitive to quasiparticle jumps and only one transition line is observed. Equation (2) in main text, indeed, gives no dependence of the transition frequency on the modulation amplitude. Accurate numerics, plotted as a dashed line, however, displays some dependence owing to deviations from simple sinusoidal charge dispersion. Due to strong  $1/f$  charge noise when off the gate charge sweet spot ( $n_0 = 0; 0.5$ ), the transition peak as well as the phonon sidebands are nearly absent except at the dynamical sweet spots (see Fig. S5b).



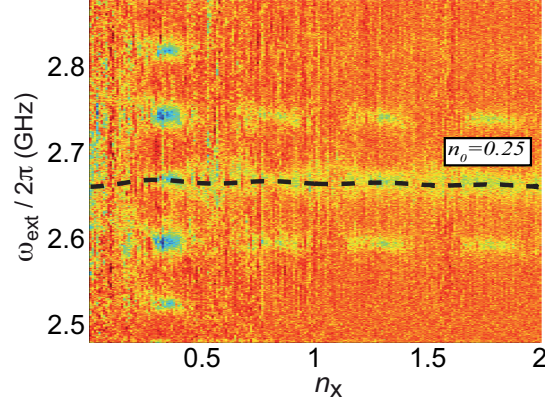


FIG. S3: **Phonon Stark shift.** Similar to Fig. 2d in main text, but the gate offset is set to the maximum slope,  $n_0 = 0.25$ , of the modulation curve. The measured population of  $|f\rangle$  is proportional to the color code. At this gate offset, the Stark shift is minimal as expected from both analytics and numerics. The dashed line is from full numerical Floquet modeling.

## THEORETICAL DETAILS

### Hamiltonian

We are considering the tripartite system consisting of the transmon qubit, microwave cavity, and the mechanical resonator, as displayed in Fig. S4.

The qubit is connected to the mechanical resonator via the gate capacitance  $C_g(x)$  dependent on the displacement  $x$  of the mechanical resonator, which in the following can be either a classical variable or an operator. In the latter case, we have

$$x = x_{\text{zp}} (b^\dagger + b) . \quad (\text{S1})$$

The zero-point oscillation rms amplitude is

$$x_{\text{zp}} = \sqrt{\frac{\hbar}{2m\omega_m}} .$$

The displacement gives rise to a motional gate charge defined as

$$n_x = \frac{dC_g(x)}{dx} \frac{V_{\text{dc}}}{2e} x . \quad (\text{S2})$$

The transmon qubit<sup>3</sup> is schematically the same as the split Cooper-pair box, consisting of a superconducting loop interrupted by two Josephson junctions with Josephson energies  $E_{J1}$  and  $E_{J2}$ . For future use, we define the total Josephson energy  $E_J$ , and the difference  $E_{J-}$ . They are tunable by the flux  $\Phi_e$  through the superconducting loop:

$$\begin{aligned} E_J(\Phi_e) &= (E_{J1} + E_{J2}) \cos\left(\pi \frac{\Phi_e}{\Phi_0}\right) \\ E_{J-}(\Phi_e) &= (E_{J1} - E_{J2}) \sin\left(\pi \frac{\Phi_e}{\Phi_0}\right) . \end{aligned} \quad (\text{S3})$$

For the moment, we linearize the dependence of the capacitance on displacement:

$$C_g(x) = C_g + \frac{dC_g(x)}{dx} x = C_g \left( 1 + \frac{C'_g}{C_g} x \right) , \quad (\text{S4})$$

where we denoted the un-displaced gate capacitance by  $C_g(x=0) \equiv C_g$ . The capacitance in parallel with the junctions is denoted by  $C_q$ , the sum of the capacitances of the individual junctions and of an interdigital capacitor.

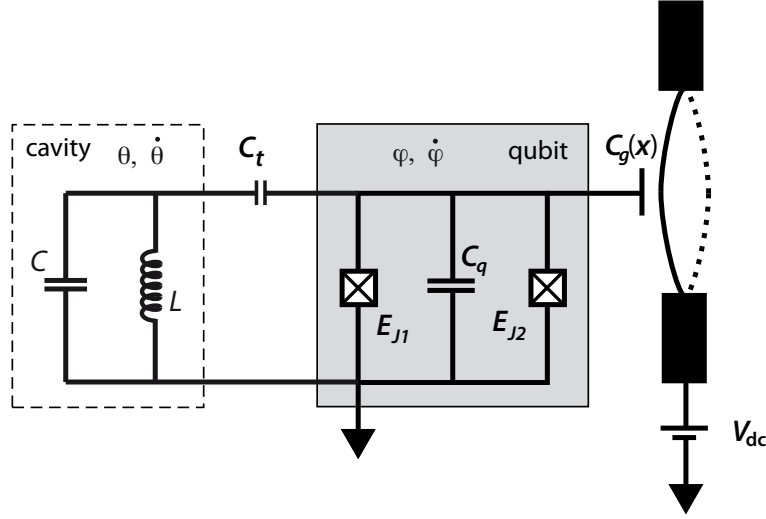


FIG. S4: Circuit schematics of a transmon qubit (shaded box) coupled capacitively to a micromechanical resonator via a gate capacitance  $C_g(x)$ , as well as to a microwave cavity represented as an  $LC$  resonator (dashed box).

The total capacitance of the qubit is the sum of  $C_q$ ,  $C_g(x)$ , and of  $C_t$  which is the coupling capacitor to cavity. The values are supposed to be related as  $C_g, C_t \ll C_q$ . The (single-electron) charging energy is

$$E_C = \frac{e^2}{2[C_q + C_g(x) + C_t]} \simeq \frac{e^2}{2C_q}.$$

Let us derive the Hamiltonian for the entire tripartite system. The canonical coordinates  $\varphi$  and  $\theta$  denote the phases of the qubit island, and of the cavity, respectively. The qubit island charge  $Q$  is related to the number of Cooper pairs  $n$  on the island as

$$Q = 2en = C_g(\dot{\varphi} - V_{dc}) + C_t(\dot{\varphi} - \dot{\theta}) + C_q\dot{\varphi}.$$

One writes down the Lagrangian which is a function of the generalized coordinates and their time derivatives. We use the subscript  $q$  for the qubit,  $c$  for the cavity, and  $m$  for the mechanical resonator. The Hamiltonian will consist of the Hamiltonians of the qubit  $H_q$ , the cavity  $H_c$ , the mechanical resonator  $H_m$ , and of their couplings. We expand in the small parameter  $\frac{C'_g}{C_g}x$ , and obtain

$$H = H_q + H_c + H_m + H_{qc} + H_{qm} + H_{cm} + H_{qcm} + H_{c2m}. \quad (\text{S5})$$

The terms are

$$\begin{aligned} H_q &= 4E_C (n - n_0)^2 - E_J \cos(\varphi) - E_{J-} \sin(\varphi) \\ H_c &= \hbar\omega_c(a^\dagger + a) \\ H_m &= \hbar\omega_m(b^\dagger + b) \\ H_{qc} &= \hbar g_c(n_0 - n)(a^\dagger + a) \\ H_{qm} &= \hbar g_m(n_0 - n)(b^\dagger + b) \\ H_{cm} &= \hbar g_{cm}(a^\dagger + a)(b^\dagger + b) \\ H_{qcm} &= \hbar g_{qcm}n(a^\dagger + a)(b^\dagger + b) \\ H_{c2m} &= \hbar g_{c2m}(a^\dagger + a)^2(b^\dagger + b), \end{aligned} \quad (\text{S6})$$

and the coupling energies read

$$\begin{aligned}
\hbar g_c &= \frac{C_c e}{C_q} \sqrt{\frac{2\hbar\omega_c}{C}} \\
\hbar g_m &= x_{zp} V_{dc} C'_g \frac{2e}{C_q} \\
\hbar g_{cm} &= \frac{x_{zp} C'_g C_c V_{dc}}{2C_q} \sqrt{\frac{2\hbar\omega_c}{C}} \\
\hbar g_{qcm} &= \frac{x_{zp} C'_g C_c e}{C_q^2} \sqrt{\frac{2\hbar\omega_c}{C}} \\
\hbar g_{c2m} &= \frac{C_c^2}{C_q^2} \frac{x_{zp} C'_g \hbar\omega_c}{2C} .
\end{aligned} \tag{S7}$$

The direct cavity-mechanics linear interaction  $H_{cm}$  is usually negligible, owing to different energy scales,  $\omega_m \ll \omega_c$ . The last term  $H_{c2m}$  in Eqs. (S6) and (S7) is a radiation-pressure interaction from the mechanics to cavity. Although generally small, it can provide a medium for finding and characterization of the mechanical resonance via the "circuit optomechanics" methods<sup>4</sup> by pumping the cavity up to photon numbers  $\gg 1$ . The second-last term  $H_{qcm}$  also becomes in the dispersive limit approximately a radiation-pressure term<sup>5</sup>, however, it becomes irrelevant since a high photon number destroys the qubit operation.

The relevant physics discussed here is thus due to the Hamiltonian of Eq. (1) in the main text,

$$H = H_q + H_c + H_m + H_{qc} + H_{qm} , \tag{S8}$$

which describes the qubit coupled to two harmonic oscillators.

Let us repeat that the above results were written under the assumption of linearization of the gate capacitance with respect to displacement of the mechanical resonator, Eq. (S4). This holds for small displacement such that the motional gate charge  $n_x$  is much less than the period of 1. However, in the experiment we reach the regime where the linearization fails. The interesting physics in this regime is detailed starting from section .

### Quantum treatment of the electromechanical coupling

The qubit-mechanics interaction part in Eq. (1) in the main text is (setting  $\hbar = 1$ )

$$H = H_q + \omega_m(b^\dagger b + 1/2) + g_m(n_0 - n)(b^\dagger + b). \tag{S9}$$

One can diagonalize the qubit, and rotate the coupling term into the qubit eigenbasis. Generally, the coupling will then have components in all three pseudospin directions. However, for this example we write it as

$$H \sim -\frac{\omega_{e-f}}{2} \sigma_z + \omega_m(b^\dagger b + 1/2) + g_m(b^\dagger + b) \sigma_x , \tag{S10}$$

which is the Jaynes-Cummings Hamiltonian. The eigenstates are dressed states, which are entangled states of the qubit states, and of the harmonic oscillator Fock states  $|N_m\rangle$  with  $N_m$  phonons:

$$\begin{aligned}
|+, N_m\rangle &= \cos\left(\frac{\Theta_N}{2}\right) |f, N_m\rangle + \sin\left(\frac{\Theta_N}{2}\right) |e, N_m + 1\rangle \\
|-, N_m\rangle &= -\sin\left(\frac{\Theta_N}{2}\right) |f, N_m\rangle + \cos\left(\frac{\Theta_N}{2}\right) |e, N_m + 1\rangle .
\end{aligned} \tag{S11}$$

Here,

$$\tan \Theta_N = \frac{2g_m \sqrt{N_m + 1}}{\Delta} , \quad \Delta = \omega_{e-f} - \omega_m \tag{S12}$$

The eigenenergies are

$$E_{\pm, N} = \omega_m(N_m + 1) \pm \frac{1}{2} \sqrt{4g_m^2(N_m + 1) + \Delta^2} . \tag{S13}$$

The degree of mixing is given by the angle  $\Theta_N$  which basically depends on the ratio of coupling to the qubit frequency, and on the number of phonons. By increasing the phonon number, therefore, the eigenstates can attain a highly mixed character. Another way to indicate the increased coupling with higher Fock states is that from Eq. (S12), (S13) one sees that an effective coupling is

$$g^* = g_m \sqrt{N_m + 1},$$

which in the present case, given a maximum about  $N_m \sim 2 \times 10^6$ , would exceed the qubit frequency.

The discussion starting from Eq. (S9) assumes the validity of the linearized interaction Eq. (S4), however, this assumption does not hold any more when the motional gate charge becomes comparable to about  $n_x \gtrsim 0.1$ . A rough estimate for the mixing angle is then given by using for the effective coupling the amplitude for the transmon charge dispersion, see below Eq. (S25), *viz.*,  $g^* \sim \epsilon_n \sim 200$  MHz. We then obtain that the dressing of the eigenstates remains quite moderate, at the level of  $\sim 10\%$  in the experiment. In the first approximation, the eigenstates are hence states with the qubit in either  $|e\rangle$  or  $|f\rangle$ , and the mechanical resonator with a certain  $N_m$  number of quanta.

In order to treat effects beyond the linear regime, we will consider the coupling of the qubit to the mechanical resonator semiclassically, *i.e.*, treating the latter as a classical field coupling to the qubit:

$$n_g(t) = n_0 + n_x \cos(\omega_g t). \quad (\text{S14})$$

This is the starting point for the rest of this Supplementary.

### Charge qubit approximation

In the basis of number states, the general Hamiltonian of the split Cooper-pair box, or transmon, reads

$$H_q = \sum_n \left\{ 4E_C (n - n_g)^2 |n\rangle - \frac{1}{2} E_J (|n+1\rangle + |n-1\rangle) - \frac{i}{2} E_{J-} (|n+1\rangle - |n-1\rangle) \right\} \langle n|. \quad (\text{S15})$$

Let us first consider the case of a charge qubit, which has  $E_C \gtrsim E_J$ . Although the transmon qubit operates in the extreme limit  $E_C \ll E_J$ , the present discussion provides, nonetheless, useful insight. For the moment, we ignore the asymmetry of the Josephson energies.

Restricting to a subspace involving two states, Eq. (S15) can be written using the Pauli matrices. With the two lowest-energy states  $n = 0, 1$ , as well as  $n_g$  between 0 and  $-1/2$ , we obtain

$$H_{01} = -2E_C(1 + 2n_g)\sigma_z - \frac{1}{2}E_J\sigma_x. \quad (\text{S16})$$

The Hamiltonian  $H_{01}$  has the eigenstates  $|g\rangle$  and  $|e\rangle$ , the ground state and the first excited state, respectively. Of most interest for the present work is the next higher transition:

$$H_{12} = -8E_C n_g \sigma_z - \frac{1}{2} E_J \sigma_x, \quad (\text{S17})$$

which has the eigenstates  $|e\rangle$  and  $|f\rangle$ . Hence, the effective charging energy, and thus the charge dispersion of the energy, is enhanced by a factor of two by considering the first excited and second excited charge states. Generally, it grows by a factor of two for each higher transition in the charge qubit model. Notice that the gate charge periodicity in Eq. (S17) is offset by half a period with respect to the lowest transition, Eq. (S16).

We swap the  $z$  and  $x$  spin indices in Eq. (S16), for the purpose of following the standard that the spin is pointing along the  $z$  axis. The coupling of the driving field via charging energy is then perpendicular to the pseudospin direction. The two-charge state Hamiltonian describing the ground and first excited states  $g$  and  $e$  is:

$$H_{01} = -\frac{1}{2} E_J \sigma_z - 2E_C(1 + 2n_g)\sigma_x, \quad (\text{S18})$$

with  $n_g$  between 0 and  $-1/2$ , see Fig. S5a. Beyond these values setting the limits of the linear regime (in the charge qubit case), the charging energy is periodic. We can approximate this dependence as sinusoidal, such that Eq. (S18) becomes

$$H_{01} \simeq -\frac{1}{2} E_J \sigma_z - E_c [1 + \cos(2\pi n_g)] \sigma_x. \quad (\text{S19})$$

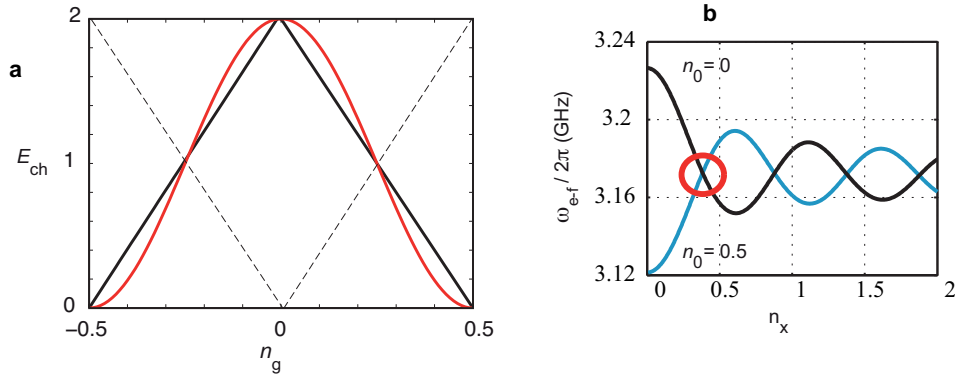


FIG. S5: **Charging energy of the qubit.** **a**, Charging energy for the two lowest charge states in Eq. (S16) (black solid line), and a sinusoidal approximation of it (red, Eq. (S19)). The dashed lines depict the presence of an extra quasiparticle on the island. The y-axis is scaled with  $E_C$  and x-axis is the gate charge. **b**, Illustration of a "dynamical sweet spot", where the qubit level spacing at a certain modulation amplitude is insensitive to changes in the offset charge  $n_0$ . The lines depicting the level spacings cross, independently of  $n_0$ , for the first time at about  $n_x \simeq 0.4$ .

Using Eq. (S14), we obtain all harmonics by the Bessel expansion of the sinusoid of a sinusoid, while the dominant term is time-independent:

$$H_{01} \simeq -\frac{1}{2}E_J\sigma_z - E_c\left\{1 + \cos(2\pi n_0)J_0(2\pi n_x)\right\}\sigma_x. \quad (\text{S20})$$

The difference between level spacings of Eq. (S20) and that of the uncoupled qubit, Eq. (S19) with  $n_g(t) = n_0$ , yields the Stark shift for the transition between the ground state  $g$  and the first excited state  $e$ :

$$\Delta\omega_{g-e} \simeq \frac{2E_C^2}{E_J} \left[ 2\cos(2\pi n_0)(J_0(2\pi n_x) - 1) + \cos^2(2\pi n_0)(J_0^2(2\pi n_x) - 1) \right]. \quad (\text{S21})$$

Similar to Eq. (S19), we can approximate the higher transition Eq. (S17)

$$H_{12} \simeq -\frac{E_J}{2}\sigma_z - 2E_c[1 - \cos(2\pi n_g)]\sigma_x \quad (\text{S22})$$

and we obtain a Stark shift for the next higher pair of states  $e$  and  $f$ , enhanced by a factor of 4 over Eq. (S21):

$$\Delta\omega_{e-f} \simeq \frac{8E_C^2}{E_J} \left[ -2\cos(2\pi n_0)(J_0(2\pi n_x) - 1) + \cos^2(2\pi n_0)(J_0^2(2\pi n_x) - 1) \right]. \quad (\text{S23})$$

The results in Eqs. (S21), (S23) arise from a simplified model of treating the transmon as a charge qubit, although the parameter regime  $E_J/E_C$  of these two are in fact the opposite limits. However, the results are qualitatively correct, as seen in Fig. S6. This is mostly due to the fact that the charge dispersion for the higher transition (see section ) is relatively correctly predicted.

In the experiment, we also observe the effect of a quasiparticle which intermittently tunnels in and out of the island. The presence of the quasiparticle shifts the charging energy by half a period, see Fig. S5a. Therefore, in a time-averaged measurement, two gate charge values differing by one electron appear as superimposed on top of each other. This behavior is rather typically observed in circuits where the single-electron charging effects are noticeable<sup>6</sup>. As it is often the case in superconducting devices, the origin of the quasiparticles is somewhat unclear, but can be associated with radiation from higher-temperature parts of the experimental setup.

#### Using the charge dispersion of the transmon qubit

The charge dispersion of the transmon is derived in the limit  $E_J \gg E_C^3$ . Here, for convenience we use numeric labels  $n = 0, 1, 2, \dots$  for the eigenstates (not to be confused with number states used in sections , ). The eigenenergies are

$$\omega_n(n_g) = \omega_n(n_g = 1/4) - \frac{\epsilon_n}{2} \cos(2\pi n_g). \quad (\text{S24})$$



The peak-to-peak amplitude is

$$\epsilon_n = (-1)^n E_C \frac{2^{4n+5}}{n!} \sqrt{\frac{2}{\pi}} \left( \frac{E_J}{2E_C} \right)^{\frac{n}{2} + \frac{3}{4}} \exp \left( -\sqrt{8E_J/E_C} \right). \quad (\text{S25})$$

Since the higher levels have progressively stronger charge dispersion, a good approximation for the transition energies between two levels is given by  $\omega_{n-1,n} \simeq \omega_n$ .

Let us take the gate dependence as a slow modulation of the level energy in the eigenbasis, and, for simplicity, label  $\omega_0 \equiv \omega_n(n_g = 1/4)$ . We use the previous notation for the Pauli matrices which operate now in the eigenbasis,

$$H_q = -\frac{1}{2} [\omega_0 + \epsilon_2 \cos(2\pi n_g(t))] \sigma_z \quad (\text{S26})$$

where  $n_g(t)$  is given by Eq. (S14). In the same way as starting from Eq. (S19) in the charge-qubit model in section , we use a Bessel expansion to break this into multiple frequencies. However, in contrast to the simplistic model, we now include all frequencies:

$$H_q = -\frac{1}{2} \delta_0 \sigma_z - \frac{1}{2} \sum_{\beta=1} \delta_\beta \cos(\beta \omega_g t) \sigma_z \quad (\text{S27})$$

where

$$\begin{aligned} \delta_0 &= \omega_0 + \frac{\epsilon_2}{2} \cos(2\pi n_0) J_0(2\pi n_x) \\ \delta_\beta &= (-1)^{\beta/2} \epsilon_2 \cos(2\pi n_0) J_\beta(2\pi n_x), \quad \text{even } \beta \\ \delta_\beta &= (-1)^{(\beta+1)/2} \epsilon_2 \sin(2\pi n_0) J_\beta(2\pi n_x), \quad \text{odd } \beta \end{aligned} \quad (\text{S28})$$

### Spectroscopy by the excitation microwave

#### First sidebands

Let us consider as an introductory example a two-level Hamiltonian in its eigenbasis, coupled to *two* linearly polarized fields:

$$H_q = -\frac{1}{2} [\delta_0 + \delta \cos(\omega_g t)] \sigma_z - g_{\text{ext}} \cos(\omega_{\text{ext}} t) \sigma_x. \quad (\text{S29})$$

The (low-frequency) field with frequency  $\omega_g$  and Rabi frequency  $\delta$  will describe the (strong) drive due to the phonon field, and the perpendicular field having the frequency  $\omega_{\text{ext}}$  and Rabi frequency  $g_{\text{ext}}$  models the excitation tone in two-tone spectroscopy. The probe tone used to measure the qubit state via dispersive cavity readout is not considered; it simply gives a phase shift proportional to the population of the upper level.

We move to a non-uniformly rotating frame with respect to the mechanical modulation by the transformation

$$u = \exp \left[ i \frac{\delta}{2\omega_g} \sin(\omega_g t) \sigma_z \right]. \quad (\text{S30})$$

We obtain

$$H_q = -\frac{\delta_0}{2} \sigma_z - \sum_{k=-\infty}^{\infty} \Delta_{2k} \cos[(\omega_{\text{ext}} + 2k\omega_g)t] \sigma_x + \sum_{k=-\infty}^{\infty} \Delta_{2k-1} \sin[\omega_{\text{ext}} + (2k-1)\omega_g t] \sigma_y. \quad (\text{S31})$$

The Rabi frequencies are

$$\Delta_k = g_{\text{ext}} J_k \left( \frac{\delta}{\omega_m} \right). \quad (\text{S32})$$

*Strong drive*

In reality the situation is more complex, since our two-level system (TLS) is coupled to a sum of fields having different frequencies, which are due to expanding the sine of sine (Eq. (S27)), and also to the excitation tone:

$$H_q = -\frac{1}{2} \left[ \delta_0 + \sum_{\beta=1}^{\infty} \delta_{\beta} \cos(\beta\omega_g t) \right] \sigma_z - g_{\text{ext}} \cos(\omega_{\text{ext}} t) \sigma_x. \quad (\text{S33})$$

Here, one has to repeat the transformation  $u$  of Eq. (S30) separately for each frequency component, yielding the overall transformation:

$$U = \exp \left[ \frac{i\sigma_z}{2} \sum_{\beta=1}^{\infty} \frac{\delta_{\beta}}{\beta\omega_g} \sin(\beta\omega_g t) \right]. \quad (\text{S34})$$

Equation (S33) becomes

$$H_q = -\frac{1}{2} \delta_0 \sigma_z - \frac{g_{\text{ext}}}{2} \cos(\omega_{\text{ext}} t) (P + P^*) \sigma_x - \frac{ig_{\text{ext}}}{2} \cos(\omega_{\text{ext}} t) (P - P^*) \sigma_y, \quad (\text{S35})$$

where we used the shorthand notation

$$P \equiv \exp \left[ i \sum_{\beta=1}^{\infty} \frac{\delta_{\beta}}{\beta\omega_g} \sin(\beta\omega_g t) \right]. \quad (\text{S36})$$

Let us also define  $\delta'_{\beta} \equiv \frac{\delta_{\beta}}{\beta\omega_g}$ . With further algebra we get

$$\begin{aligned} P^* &\Rightarrow \sum_{p=-\infty}^{\infty} J_p \left( \frac{\delta_1}{\omega} \right) \exp(-ip\omega_g t) \times \sum_{q=-\infty}^{\infty} J_q \left( \frac{\delta_2}{2\omega} \right) \exp(-2iq\omega_g t) \times \dots \\ &= \left\{ \dots + J_{-1}(\delta'_1) \exp(i\omega_g t) + J_0(\delta'_1) + J_1(\delta'_1) \exp(-i\omega_g t) + J_2(\delta'_1) \exp(-2i\omega_g t) + \dots \right\} \times \\ &\times \left\{ \dots + J_{-1}(\delta'_2) \exp(2i\omega_g t) + J_0(\delta'_2) + J_1(\delta'_2) \exp(-2i\omega_g t) + J_2(\delta'_2) \exp(-4i\omega_g t) + \dots \right\} \times \\ &\times \dots \end{aligned} \quad (\text{S37})$$

We neglect sidebands of sidebands, since they have a lower amplitude. Then the explicitly written two lines in Eq. (S37) yield multiples of the mechanical frequency up to third order:

$$P^* \simeq J_0(\delta'_1) J_0(\delta'_2) - 2iJ_1(\delta'_1) J_0(\delta'_2) \sin(\omega_g t) - 2iJ_1(\delta'_2) J_0(\delta'_1) \sin(2\omega_g t) - 2iJ_1(\delta'_3) J_0(\delta'_2) \sin(3\omega_g t) + \dots \quad (\text{S38})$$

This result is applied in Eq. (S35), obtaining

$$\begin{aligned} H_q &= -\frac{1}{2} \delta_0 \sigma_z - \Delta_0 \cos(\omega_{\text{ext}} t) \sigma_x - \Delta_1 [\sin(\omega_{\text{ext}} + \omega_g t) - \sin(\omega_{\text{ext}} - \omega_g t)] \sigma_y + \\ &+ \Delta_2 [\sin(\omega_{\text{ext}} + 2\omega_g t) - \sin(\omega_{\text{ext}} - 2\omega_g t)] \sigma_y + \dots \end{aligned} \quad (\text{S39})$$

The Rabi frequencies are now

$$\begin{aligned} \Delta_0 &= g_{\text{ext}} J_0 \left( \frac{\delta_1}{\omega_g} \right) J_0 \left( \frac{\delta_2}{2\omega_g} \right) \\ \Delta_1 &= g_{\text{ext}} J_1 \left( \frac{\delta_1}{\omega_g} \right) J_0 \left( \frac{\delta_2}{2\omega_g} \right) \\ \Delta_2 &= g_{\text{ext}} J_1 \left( \frac{\delta_2}{2\omega_g} \right) J_0 \left( \frac{\delta_1}{\omega_g} \right) \\ \Delta_3 &= g_{\text{ext}} J_1 \left( \frac{\delta_3}{3\omega_g} \right) J_0 \left( \frac{\delta_2}{2\omega_g} \right). \end{aligned} \quad (\text{S40})$$

The higher Rabi frequencies ( $k > 1$ ) are suppressed from those in Eq. (S32), nearly comparable to that of the main peak ( $k = 0$ ), due to the nested Bessel function dependence.

### Level populations

One can estimate the populations of the qubit levels in the spectroscopy experiment discussed in section . Let us consider a generic TLS described by a spin Hamiltonian, with a notation reminiscent of this discussion:

$$H_q = -\frac{\delta_0}{2}\sigma_z - \frac{\Delta_x}{2}\sigma_x - \frac{\Delta_y}{2}\sigma_y. \quad (\text{S41})$$

This Hamiltonian is time-independent, however, in a rotating frame, a driven system will adopt similar form. For notational simplicity, let 0 and 1 denote the ground and first excited states of the TLS.

The Liouvillean master equation for the density matrix is:

$$\dot{\rho} = \frac{1}{i\hbar} [H, \rho] + \mathcal{L}[\rho], \quad (\text{S42})$$

where the Liouvillean with decay and pure dephasing is:

$$\mathcal{L}[\rho] = -\frac{\gamma}{2} (\sigma^+ \sigma^- \rho + \rho \sigma^+ \sigma^- - 2\sigma^- \rho \sigma^+) + \frac{\gamma_\varphi}{2} (\sigma_z \rho \sigma_z - \rho). \quad (\text{S43})$$

The steady-state population of the excited state in the Rotating-Wave Approximation becomes

$$\rho_{11} = 1 - \rho_{00} = \frac{\frac{\gamma_{\text{tot}}}{2\gamma} (\Delta_x^2 + \Delta_y^2)}{\delta_0^2 + \frac{\gamma_{\text{tot}}}{\gamma} (\Delta_x^2 + \Delta_y^2) + \gamma_{\text{tot}}^2}, \quad (\text{S44})$$

Here, the total decoherence rate is

$$\gamma_{\text{tot}} = \frac{\gamma}{2} + \gamma_\phi. \quad (\text{S45})$$

Equation (S44) is Lorentzian having the full width at half maximum

$$\delta\omega = 2\sqrt{(\Delta_x^2 + \Delta_y^2) \frac{\gamma_{\text{tot}}}{\gamma} + \gamma_{\text{tot}}^2}. \quad (\text{S46})$$

In order to apply these results for the Hamiltonians Eq. (S31), (S39) describing the spectroscopy experiment, we make another transformation  $u_2 = \exp[-i(\omega_{\text{ext}} + k\omega_g)t\sigma_z/2]$  into a frame rotating with a particular sideband  $k = -\infty \dots \infty$ . We can then use Eq. (S44) for finding the steady-state population. One next makes the  $u_2$  transformation into the frame of each of the sidebands separately. If the peaks do not overlap, i.e.,  $\delta\omega \ll \omega_m$ , one can sum the occupancies due to each such operation:

$$\rho_{11} = \frac{1}{2} \sum_{k=-\infty}^{\infty} \frac{\gamma_{\text{tot}} \Delta_k^2}{\gamma(\delta_0 - \omega_{\text{ext}} - k\omega_g)^2 + \gamma_{\text{tot}}(\Delta_k^2 + \gamma\gamma_{\text{tot}})}, \quad (\text{S47})$$

where the Rabi frequencies are given either by Eq. (S32) for the case of weak drive, or, more generally by Eq. (S40). In the latter case, the sideband Rabi frequencies are suppressed from those in Eq. (S32) due to the nested Bessel function dependence.

Using these results, we can plot a prediction for the oscillatory Stark shift whose measurement data was shown Fig. 2d in the main text. We obtain an excellent agreement, as displayed in Fig. S6. The mirrored image is missing in the simulation since we have not included the offset quasiparticle in the simulation. The sideband visibility, proportional to its Rabi frequency, undulates with increasing  $n_x$  according to the nested Bessel function dependence.

### Floquet calculation of the driven transmon

According to the Floquet theorem<sup>7,8</sup>, the time-dependent Schrödinger equation,

$$H(t)|\Psi(t)\rangle = i\hbar\partial_t|\Psi(t)\rangle, \quad (\text{S48})$$

with a time-periodic Hamiltonian,  $H(t) = H(t+T)$ , has a solution

$$|\Psi_\alpha(t)\rangle = |u_\alpha(t)\rangle e^{-i\varepsilon_\alpha t/\hbar}, \quad (\text{S49})$$

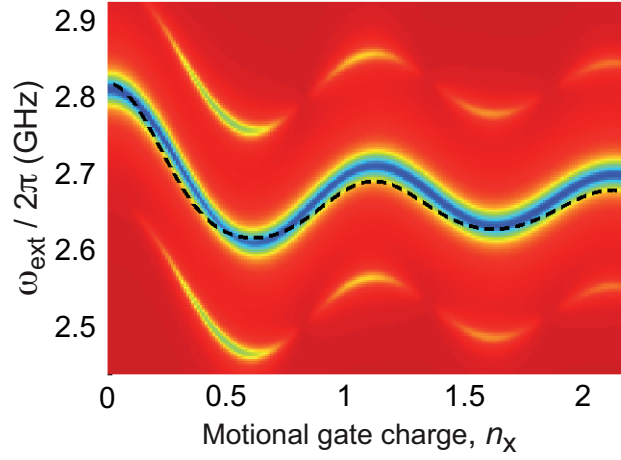


FIG. S6: **Analytical model of Fig. 2d in main text.** The dashed line is the charge-qubit limit prediction, Eq. (S23), however, with unrealistically low  $E_J(\Phi_{\text{dc}}/\Phi_0 = 0.370) = 6.0$  GHz. This is due to that the charge qubit model exaggerates the charge dispersion in the current transmon limit  $E_J \gtrsim E_C$ .

where  $|u_\alpha(t)\rangle$  is periodic in time with period  $T = 2\pi/\omega$ . Substituting Eq. (S49) into Eq. (S48), we obtain the equation for the quasienergy state  $|u_\alpha(t)\rangle$ ,

$$[H(t) - \varepsilon_\alpha] |u_\alpha(t)\rangle = i\hbar\partial_t |u_\alpha(t)\rangle, \quad (\text{S50})$$

which is just the time-dependent Schrödinger equation with the energy shifted by the quasienergy  $\varepsilon_\alpha$ .

We expand the Hamiltonian and the quasienergy state with their Fourier components as

$$H(t) = \sum_n \sum_{\alpha,\beta} h_{\alpha\beta}^n e^{in\omega t} |\alpha\rangle\langle\beta|, \quad (\text{S51})$$

$$|u(t)\rangle = \sum_m \sum_\alpha c_\alpha^m e^{im\omega t} |\alpha\rangle. \quad (\text{S52})$$

Plugging these into Eq. (S50) yields

$$\sum_m \sum_\beta \left( h_{\alpha\beta}^{n-m} + \delta_{n,m} \delta_{\alpha,\beta} m\hbar\omega \right) c_\beta^m = \varepsilon_\alpha c_\alpha^n. \quad (\text{S53})$$

Defining the Floquet matrix  $H_F$  as

$$\langle \alpha n | H_F | \beta m \rangle = h_{\alpha\beta}^{n-m} + m\hbar\omega \delta_{n,m} \delta_{\alpha,\beta}, \quad (\text{S54})$$

this eigenvalue problem can be written in a simple matrix form

$$H_F \vec{c} = \varepsilon \vec{c}. \quad (\text{S55})$$

Thus, we have transformed the finite-dimensional time-dependent problem to an infinite-dimensional time-independent problem. However, the number of Floquet blocks can be truncated depending on the strength of the periodic drive leading to computable eigenvalue problem.

The Hamiltonian we consider is given in the Cooper pair basis by the qubit Hamiltonian (Eq. (S15)) with the gate charge driven sinusoidally, viz. Eq. (S14). This procedure allows for an exact treatment of the transmon qubit. The Fourier components of the Hamiltonian are

$$H^{[0]} = H_q, \quad (\text{S56})$$

$$H^{[\pm 1]} = 4E_C (n_0 - n) n_x. \quad (\text{S57})$$

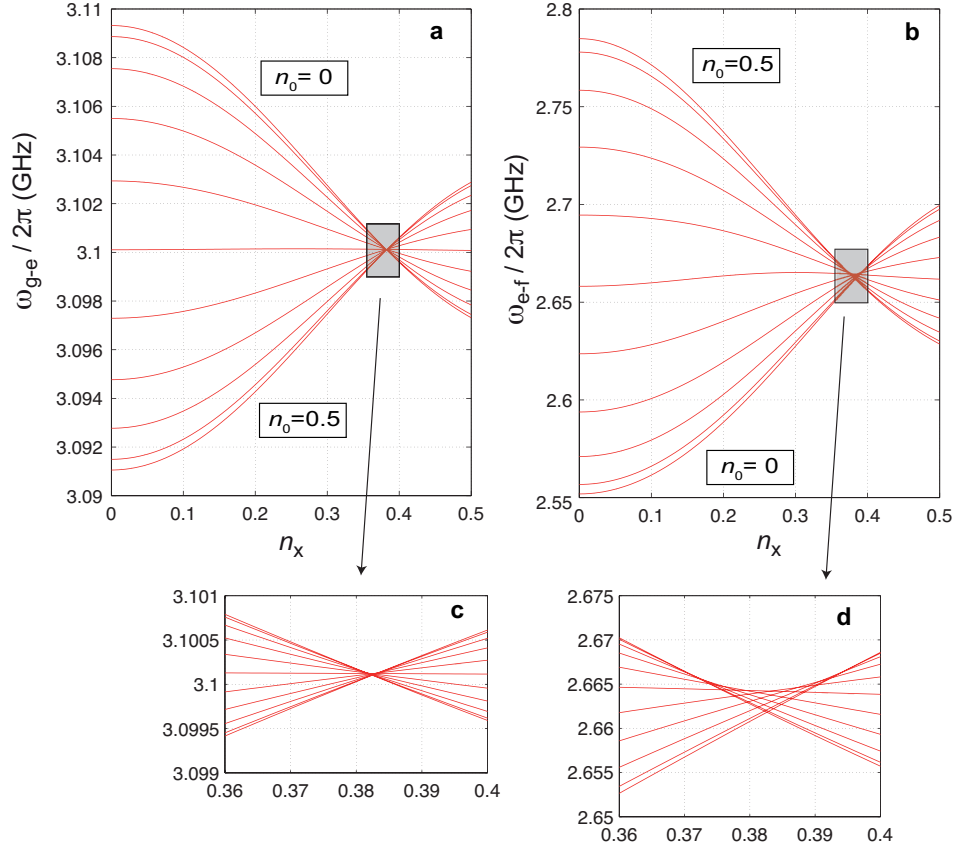


FIG. S7: **Floquet results of the dynamical sweet spot.** **a**, Transition frequency between the ground state and first excited state, as a function of gate charge modulation amplitude. **b**, Transition between the first and second excited states. **c,d**, Zoom-in of the regions marked in **a,b**, respectively. The family of curves depict changing  $n_0$  in steps of 0.05 between 0 and 1/2 as labelled. Notice the different scales in all panels.

The Floquet Hamiltonian is thus given by

$$H_F = \begin{pmatrix} \ddots & & & & \\ & \ddots & & & \\ & & H^{[0]} - \omega \hat{I} & H^{[-1]} & \\ & & H^{[+1]} & H^{[0]} & H^{[-1]} \\ & & & H^{[+1]} & H^{[0]} + \omega \hat{I} & \ddots \\ & & & & & \ddots & \ddots \end{pmatrix}, \quad (\text{S58})$$

where the dimension of  $H^{[0]}$  and  $H^{[\pm 1]}$  is given by the number of Cooper pair number states used. In the modeling presented, 41 Cooper pair number states were used with 201 Floquet states. The size of the Floquet matrix was therefore  $8241 \times 8241$ .

The transition frequencies plotted in Fig. 2d in main text and in Fig. S3, are then obtained as a difference of a proper pair of quasienergies<sup>9</sup>. We can also inspect the dynamical sweet spot (see also Fig. S5) in more detail, as displayed in Fig. S7. For the lowest transition, the set of curves corresponding to different offset  $n_0$  cross at the same point at 0.2 % accuracy, whereas the next higher transition, the remaining dispersion is about 1 %.

In order to obtain a numerically exact solution for the qubit population, one could in principle include the qubit excitation tone in the Floquet analysis as well, however, the straightforward diagonalization becomes intractable.



### Driven response of the mechanical resonator

With both dc and ac voltage applied to the mechanical resonator

$$V_g(t) = V_{\text{dc}} + V_{\text{ac}} \cos(\omega_g t), \quad (\text{S59})$$

the driving force acting on it is

$$F = \frac{d}{dx} \left( \frac{1}{2} C_g(x) V_g^2 \right) = |F| \cos(\omega_g t), \quad (\text{S60})$$

where

$$|F| = V_{\text{dc}} V_{\text{ac}} \frac{dC_g}{dx}.$$

The induced motion is

$$x(t) = \frac{|F| \cos(\omega_g t + \Theta)}{m \sqrt{\omega_g^2 \omega_m^2 / Q_m^2 + (\omega_g^2 - \omega_m^2)^2}} \equiv |x| \cos(\omega_g t + \Theta), \quad (\text{S61})$$

where

$$\tan \Theta = \frac{\omega_m \omega_g}{Q_m (\omega_m^2 - \omega_g^2)}. \quad (\text{S62})$$

The gate charge due to the applied  $V_g$  is

$$\begin{aligned} n_g(t) &= \frac{C_g(t) V_g(t)}{2e} \simeq n_0 + \frac{dC_g}{dx} \frac{V_{\text{dc}}}{2e} |x| \cos(\omega_g t + \Theta) + \frac{C_g V_{\text{ac}}}{2e} \cos(\omega_g t) \\ &\equiv n_0 + n_x \cos(\omega_g t + \Theta) + n_v \cos(\omega_g t) = n_0 + r \cos(\omega_g t + \theta). \end{aligned} \quad (\text{S63})$$

which has been expressed as a single sinusoid on the last line with

$$r = \sqrt{n_v^2 + n_x^2 + 2n_v n_x \cos \Theta}, \quad (\text{S64})$$

and

$$\tan \theta = -\frac{n_x \sin \Theta}{n_v + n_x \cos \Theta}. \quad (\text{S65})$$

The phase shift  $\Theta$  of motion with respect to the driving voltage appears as an asymmetry in the Stark shifts in Fig. 2 in the main text.

One also obtains a relation between the motional gate charge and phonon number  $N_m = m\omega_m x_{\text{rms}}^2 / \hbar$ ,

$$N_m = \left( \frac{4E_C}{\hbar g_m} \right)^2 n_x^2. \quad (\text{S66})$$

The Stark shift, Eq. (2) in the main text, is at low phonon number

$$\Delta\omega_{\text{e-f}}/2\pi \simeq \frac{\epsilon_{\text{e-f}}}{2} \pi^2 \cos(2\pi n_0) \left( \frac{\hbar g_m}{4E_C} \right)^2 N_m. \quad (\text{S67})$$

---

\* Present address: Korea Research Institute of Standards and Science, Daejeon 305-340, Republic of Korea

† Present address: Department of Applied Physics, Aalto University School of Science, P.O. Box 11100, FI-00076 Aalto, Finland

[1] Sulkko, J. *et al.* Strong Gate Coupling of High-Q Nanomechanical Resonators. *Nano Lett.* **10**, 4884–4889 (2010).

[2] Teufel, J. D. *et al.* Circuit cavity electromechanics in the strong-coupling regime. *Nature* **471**, 204–208 (2011).

- [3] Koch, J. *et al.* Charge-insensitive qubit design derived from the Cooper pair box. *Phys. Rev. A* **76**, 042319 (2007).
  - [4] Regal, C. A., Teufel, J. D. & Lehnert, K. W. Measuring nanomechanical motion with a microwave cavity interferometer. *Nature Physics* **4**, 555–560 (2008).
  - [5] Blencowe, M. P. & Armour, A. D. Probing the quantum coherence of a nanomechanical resonator using a superconducting qubit: II. implementation. *New Journal of Physics* **10**, 095005 (2008).
  - [6] Aumentado, J., Keller, M. W., Martinis, J. M. & Devoret, M. H. Nonequilibrium Quasiparticles and  $2e$  Periodicity in Single-Cooper-Pair Transistors. *Phys. Rev. Lett.* **92**, 066802 (2004).
  - [7] Shirley, J. H. Solution of the Schrödinger Equation with a Hamiltonian Periodic in Time. *Phys. Rev.* **138**, B979–B987 (1965).
  - [8] Son, S.-K., Han, S. & Chu, S.-I. Floquet formulation for the investigation of multiphoton quantum interference in a superconducting qubit driven by a strong ac field. *Phys. Rev. A* **79**, 032301 (2009).
  - [9] Tuorila, J. *et al.* Stark Effect and Generalized Bloch-Siegert Shift in a Strongly Driven Two-Level System. *Phys. Rev. Lett.* **105**, 257003 (2010).
-